Impact of filtering on photonic time-delay reservoir computing

G. Danilenko, A. Kovalev, E. Viktorov, A. Locquet, D. Citrin, D. Rontani

Impact of filtering on photonic time-delay reservoir computing

G.O. Danilenko,[1, a)] A. V. Kovalev,[1, a)] E. A. Viktorov,[1] A. Locquet,[2, 3] D. S. Citrin,[2, 3] and D. Rontani[4]
[1)]*ITMO University, 199034 Saint Petersburg, Russia*
[2)]*Georgia Tech-CNRS IRL 2958, Georgia Tech Lorraine, 57070 Metz, France*
[3)]*School of Electrical and Computer Engineering, Georgia Institute of Technology, Atlanta, GA 30332, USA*
[4)]*Chair in Photonics, LMOPS UR 4423 Laboratory, CentraleSupélec & Université de Lorraine, 57070 Metz, France*

(*Electronic mail: danilenko.gleb98@gmail.com)

(Dated: 17 January 2023)

We analyze the modification of the computational properties of a time-delay photonic reservoir computer with a change of its feedback bandwidth. For a reservoir computing configuration based on a semiconductor laser subject to filtered optoelectronic feedback, we demonstrate that bandwidth selection can lead to a flat-topped eigenvalue spectrum, for which a large number of system frequencies are weakly damped as a result of the attenuation of modulational instability by the feedback filtering. This spectral configuration allows for optimization of the reservoir in terms of its memory capacity, while its computational ability appears to be only weakly affected by the characteristics of the filter.

Photonic reservoir computers (RC) are neuro-inspired architectures with a simplified training process, which offer state-of-the-art performance in various machine-learning benchmark tasks. The rich nonlinear dynamical behaviors in photonic devices, such as laser diodes, result in a non-trivial high-dimensional mapping, which is essential to solve classification and regression tasks correctly. However, the clear dynamical origin leading to a corresponding level of performance is an arduous problem as it strongly depends on the devices' properties used in the architectures. This study presents an RC system based on a laser diode with filtered optoelectronic feedback. We are interested in how the filter's time scales interact with those of the laser to create parametric configurations of enhanced computing capability. We base our analysis on fundamental bifurcation theory and eigenspectral properties to elucidate this question. We propose a quantitative measure that characterizes the flatness of the eigenvalue spectrum and its proximity to the imaginary axis, and find it well-correlated with the system's memory capacity. This allows for optimization of the reservoir computer's memory capacity.

I. INTRODUCTION

Reservoir computing (RC) is a computational paradigm in the field of machine learning that exploits the nonlinear, high-dimensional response of a recurrent neural network (RNN) to solve complex tasks[1]. The RC's attractiveness stems from a simplified learning process, where only the network's output-layer interconnection weights are trained using convex optimization[2]. As a result, a drastic reduction in the training complexity is observed with RC compared to typical RNN-based approaches. This salient feature makes RC easier to design and implement in hardware because the precise adjustment of interconnection weights, growing quadratically with the network's size, is not required anymore. In the last decade, various physical platforms have demonstrated the potential of physical RC[3] as fast and energy-efficient computational engine using photonic[4,5], electronic[6], and spintronic devices[7].

Within the theoretical frameworks of RC, time-delay RC (TDRC) was proposed originally as an additional simplification whereby a single dynamical node can virtualize an entire spatiotemporal network in a delayed feedback loop via time-multiplexing[8]. The only downsides are a preprocessing stage to distribute the input data to the various virtual nodes in a feedback loop and a trade-off between speed and scalability. TDRC has been widely studied in photonic systems considering architectures based on lasers with all-optical[9,10] or optoelectronic (OE) feedback[11], optoelectronic oscillators (OEO)[12–14], and photonic integrated circuits with feedback[15]. Their performance and Gb/s processing bandwidth have made them prime technological candidates for telecommunication applications[16,17].

Furthermore, using photonic TDRC architectures, it is possible to include additional band-pass filtering that will impact the intrinsic node's dynamics through the nontrivial interplay of timescales. Examples of such an architecture include OEOs and laser diode subjected to OE feedback. The primary expected impact would be a change in memory capacity (*MC*), which is a measure quantifying the ability of a system to reconstruct past inputs from present RC states. However, the nature of the nonlinear interplay and the proper choice of band-pass characteristics (*i.e.* resonance frequency, damping) would have to be carefully chosen to enhance the TDRC performance.

In photonic RC systems, the performance evaluation is usually performed using exhaustive search in various 2D parameter planes or advanced model-free optimization techniques (*e.g.,* Bayesian optimization, genetic algorithms, particle swarm optimization)[18,19]. However, predicting an accurate level of performance for an RC and understanding its origin from a dynamical standpoint remains an open problem, even if, in recent years, we have gained better insight into criti-

[a)]These authors contributed equally to this work

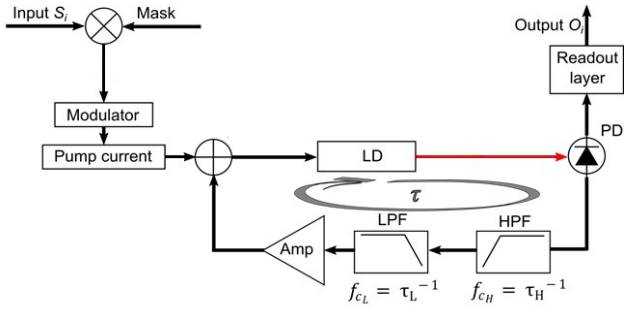

FIG. 1. Schematic setup of the photonic TDRC system based on a semiconductor laser with filtered OE feedback loop. LD, laser diode; PD, photodetector; Amp, amplifier; HPF, high-pass filter, LPF, low-pass filter. Black (red) lines are electric (optical) signals.

cal features in various types of photonic TDRC. For example, such features are the necessity to have adequate level of dynamical consistency[20], the choice of an operating point at the edge of instability (close to a bifurcation point)[11,21], regimes at the edge of injection-locking when input data is optically injected in laser with optical feedback[22].

While TDRCs allow for simple implementation of RC, it is still important to ascertain optimal performance and, moreover, to have at hand design tools by which such performance can be realized. Our focus is on evaluating the impact of feedback filtering effects on the performance of a photonic TDRC and understanding its connection with its dynamical properties. In particular, we unveil a relation between the memory capacity (*MC*) and a measure derived from the RC's eigenspectrum. Our system of interest is a semiconductor laser with a tunable bandpass filtered OE feedback. The RC's architecture and operation principle are similar to those reported previously[11], except for the the addition of low-pass filtering in the feedback loop, modelling the upper cut-off of the amplification of the electrical signal. This type of system is amongst the simplest to quantify the impact of additional filtering effects on the photonic TDRC performance. Our first observation is that the bandwidth of the bandpass filter controls the *MC* of the system. An eigenspectrum analysis reveals how the laser modulational instability characteristics can be affected by the filtering in order to improve the performance of the TDRC in terms of *MC* while preserving its computational ability.

II. MODEL

The schematic setup of the proposed photonic TDRC architecture is shown in Fig. 1. The signal detected by the photodiode is amplified and subject to tunable band-pass filtering. This signal is added to or subtracted from the injection current driving the laser, hence providing delayed OE feedback. Feeding the input data to the reservoir is realized by modulating the pump current with the signal derived from the multiplication of the input data by a mask generated from a set of uniformly distributed random numbers as defined in[11]. The impact of different types of temporal masks on the RC performance has previously been investigated in[23]. Dimensionless equations describing the system were developed based on the models in[24,25] previously used for LDs with OE feedback, in which high- and low-pass filtering of the photodetected intensity have been included:

$$\dot{I}(t) = 2N(t)I(t), \tag{1}$$

$$\dot{I}_{FH}(t) = -{\tau_H}^{-1} I_{FH}(t) + \dot{I}(t), \tag{2}$$

$$\dot{I}_{FL}(t) = -{\tau_L}^{-1}(I_{FL}(t) - I_{FH}(t)), \tag{3}$$

$$\begin{aligned}\varepsilon^{-1}\dot{N}(t) = {} & P(1+\xi M_f(t)) + \eta I_{FL}(t-\tau) - N(t) \\ & -(1+2N(t))I(t),\end{aligned} \tag{4}$$

where $I(t)$ is the normalized intensity of the laser field; $N(t)$ is the carrier density; $I_{FH}(t)$ is the high-pass filtered intensity signal and τ_H is the inverse of the high-pass filter cut-off frequency; $I_{FL}(t)$ is the low-pass filtered intensity signal and τ_L the inverse of the low-pass filter cut-off frequency; P is the pump-above-the-threshold parameter with a modulation function $M_f(t)$ for the masked input data and maximum modulation amplitude $\xi \cdot P$; η is the feedback strength (either positive or negative); τ is the feedback delay time; and ε is the ratio of the photon to the carrier lifetimes.

We consider the following set of experimentally relevant parameters, which were estimated based on the observations in[24], for further numerical analysis: $\varepsilon = 0.1$; $\tau_H = 2000$; $\tau = 1000$; $N = 48$; $\xi = 0.1$. Our choice for the number of nodes stems from the fact that for $N > 48$, the *MC* tends to saturate because the modulation frequency $1/\theta$ becomes higher than the relaxation frequency, and system's response to pump current modulation becomes damped[11]. Using $N = 48$ is relevant for the study of the particular metrics *MC* and *CA*. Time parameters are measured in the units of the photon lifetime $t_p = 10$ ps. The set of values $\tau_L = \{1, 7.5, 10\}$ is explored for the low-pass filter time-scales, corresponding to the physical cut-off frequencies 100, 13.3, 10 GHz. We should note here that the experimentally observed relaxation oscillation frequency ~ 5 GHz corresponds to 0.05 in the units of the inverse photon lifetime.

III. EIGENVALUE SPECTRUM ANALYSIS

The eigenvalues of a dynamical system provide important information about the response of the system to weak input signals or perturbations applied in different directions of phase space, which is here an infinite-dimensional functional space created by the delayed feedback. The real part of an eigenvalue corresponds to the damping rate of the response to a perturbation while the imaginary part gives the angular frequency of the oscillations in the response. Köster *et al.*[26] have demonstrated that the eigenvalues of the system's equilibrium without input, could be helpful to estimate RC performance. Specifically, they introduced the average distance reduction measure, which is analogous to an average decay time of the transients during the symbol input time. In this section, we investigate the variation of the eigenvalue spectrum of the reservoir with respect to the low-pass filtering. The characteristic

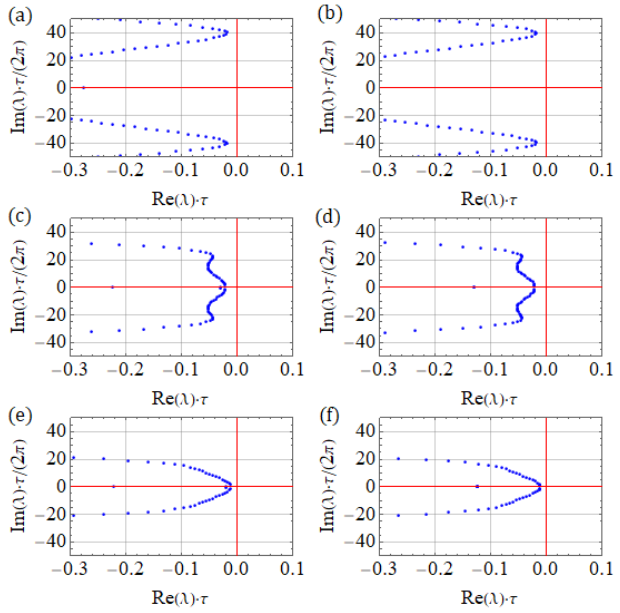

FIG. 2. Eigenvalue spectra, from top row to bottom: (a,b) τ_L = 1; (c,d) τ_L = 7.5; (e,f) τ_L = 10. The values of η and P are such that for every τ_L the system operates close to a Hopf bifurcation, and with maximal *MC*: (a) $P = 0.4$, $\eta = -0.61$; (b) $P = 0.4$, $\eta = 0.61$; (c) $P = 0.2$, $\eta = -0.98$; (d) $P = 0.2$, $\eta = 0.98$; (e) $P = 0.1$, $\eta = -0.99$; (f) $P = 0.1$, $\eta = 0.99$. The other parameters are given in the text.

equation for the system Eqs. (1)–(4) about its only non-trivial steady state $I(t) = P$, $I_{FL}(t) = I_{FH}(t) = 0$, $N(t) = 0$ reads

$$[2\varepsilon P(1+\lambda)+\lambda(\varepsilon+\lambda)](1+\tau_H\lambda)(1+\tau_L\lambda) \\ -2e^{-\lambda\tau}\eta\varepsilon P\lambda\tau_H = 0, \quad (5)$$

where λ is an eigenvalue.

We solve numerically the transcendental equation Eq. (5) and obtain the eigenvalue spectra, shown in Fig. 2 for τ_L = 1, 7.5 and 10. The three values of τ_L correspond to decreasing the low-pass cut-off frequency. We observe that close to the imaginary axis, the spectra for $\tau_L = 1$ and 10 are parabolic in the complex plane which illustrates that the real parts of the eigenvalues grow fast with the distance from the imaginary axis. For $\tau_L = 7.5$, the spectral profile in Fig. 2(c,d) is significantly different and includes a relatively large flat-topped part with a large number of weakly damped eigenvalues having a real part close to the imaginary axis. It has been shown in[26] that such a spectral profile may indicate good RC performance. The shape of the spectra suggests that there is an optimal value of the low-pass cut-off frequency for an efficient interplay between the intrinsic system's timescales, namely the relaxation oscillation (RO) frequency f_{RO} and the RO damping rate γ_{RO} of the free-running laser.

The model of Eqs. (1)–(4) accounts for the two filtering elements: high-pass and low-pass. However, the impact of the realistic high-pass filtering in our system is not found pronounced for the chosen parameters as the lower cut-off frequency remains far below, and does not interact with, the system's key frequencies. The impact of the low-pass filtering is much more pronounced.

To further investigate the relation between the eigenvalue spectrum profile and the reservoir's properties, we explore the eigenvalues in the limit of long delay (i.e. $\tau \gg 1$). This approximation, which is consistent with parameter values considered here and in the experimental implementation of OE feedback[24], allows for an analytic expression for the eigenvalue spectrum, as shown below. Following the approach in Ref. 27, we introduce the scaling

$$\lambda = \frac{\lambda_1}{\tau} + i\lambda_0, \quad (6)$$

where λ_0 and λ_1 are real numbers. Inserting of the Eq. (6) to the characteristic equation Eq. (5) and taking the leading order approximation in τ, we write the real part λ_1 of the pseudo-continuous (PC) eigenvalue spectrum as

$$\lambda_1 = J + F, \quad (7)$$

where J defines the part of the spectrum describing the modulational instability caused by the undamping of the laser RO. It reads

$$J = \ln \frac{2\varepsilon P|\eta|}{\sqrt{\varepsilon^2\lambda_0^2(1+2P)^2 + \left(\lambda_0{}^2 - 2\varepsilon P\right)^2}}, \quad (8)$$

where λ_0 is the imaginary part of the PC eigenvalue spectrum. The modulational instability has previously been considered in a semiconductor laser subject to optical feedback in the frame of the Lang-Kobayashi equation[27].

F depends only on filter characteristics and thus describes the damping of perturbations due to the filtering in the feedback loop; it is given by

$$F = \ln \frac{\tau_H|\lambda_0|}{\sqrt{\left(1+\lambda_0{}^2\tau_H{}^2\right)\left(1+\lambda_0{}^2\tau_L{}^2\right)}}. \quad (9)$$

As expected, the filtering effect is diminished ($F \to 0$) when the filter high-pass filter cut-off frequency is large ($\tau_H \gg 1$) and low-pass filter cut-off frequency is small ($\tau_L \ll 1$).

The PC spectrum is symmetric with respect to the real axis and independent of the sign of feedback strength η. The decomposition of the PC spectrum is illustrated in Fig. 3 for the three values of τ_L considered for Fig. 2. The part J, which characterizes the modulational instability, has a characteristic resonant shape reminiscent of an under-damped harmonic oscillator. The bifurcation frequency $\hat{\lambda}_0$, which aggregates the relaxation-oscillation frequency and its damping rate and corresponds approximately to the frequency at which J reaches its maximum, was obtained in[24] and is given by

$$\hat{\lambda}_0 = \sqrt{\omega_{RO}^2 - \gamma_{RO}^2}, \quad (10)$$

where $\omega_{RO} = 2\pi f_{RO} = \frac{1}{2}\sqrt{8\varepsilon P - \varepsilon^2(1+2P)^2}$ is the RO angular frequency of the free-running laser ($\eta = 0$), and $\gamma_{RO} = \frac{1}{2}\varepsilon(1+2P)$, see[25].

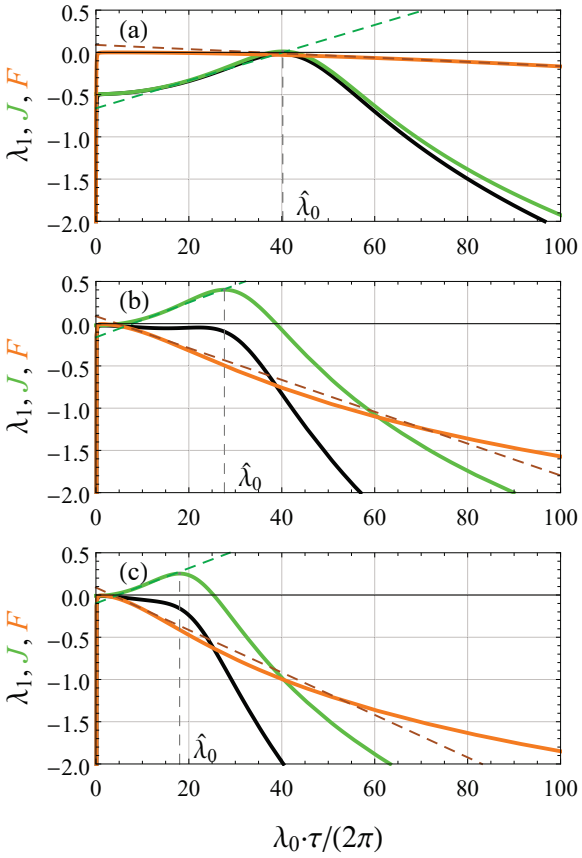

FIG. 3. Decomposition of a PC spectrum real part λ_1 (black line) into the part J defining a modulational instability caused by the relaxation oscillations undamping (green line, Eq. (8)) and the part F accounting for filtering (orange line, Eq. (9)). The dashed grey line shows the position of the J function maximum at $\hat{\lambda}_0$. The dashed green (orange) line shows a slope of a curve J (F) at the point $\hat{\lambda}_0/2$ ($1/(2\tau_L)$) for illustrative purposes. The parameters are: (a) $P = 0.4$, $\eta = 0.61$, $\tau_L = 1$; (b) $P = 0.2$, $\eta = 0.98$, $\tau_L = 7.5$; (c) $P = 0.1$, $\eta = 0.99$, $\tau_L = 10$. The other parameters are given in the text.

The part F, on the other hand, has the typical shape of a low-pass filter. For $\tau_L = 1$ (Fig. 3(a)), the cut-off is much larger than the bifurcation frequency and the effect of filtering is minor. For the two other values of τ_L, the cut-off is lower than $\hat{\lambda}_0$, and filtering modifies significantly the spectrum of the eigenvalues, as observed in Figs. 3(b,c). The flattening of the eigenvalue spectrum results from the interplay between the intrinsic system's timescales related to J and F. The term F provides the perturbation damping resulting from the filtering which can be described by a negative slope, while the part J has a positive slope determined by the modulational instability. Both slopes can be observed in Fig. 3. The optimal flattening occurs when the two slopes have similar absolute value. As a result, the filter leads to significant modification of the damping timescales, and therefore of the small signal response of the system, manifested by the appearance of a large number of eigenvalues having nearly equal real parts. We conclude that the flattening condition, and therefore, RC

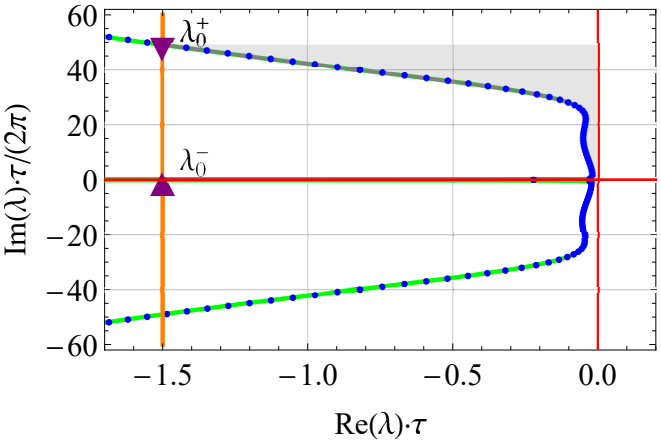

FIG. 4. Graphical representation of the average distance D defined by Eq. 11. The green line is the PC spectrum given by Eq. 7, where $\lambda_1 = Re(\lambda)\tau$, which approximates the numerical eigenvalues (blue dots) very well. Orange line is $Re(\lambda)\tau = -1.5$. Purple triangles denote the points at the PC spectrum corresponding to λ_0^- and λ_0^+ defining the averaging interval where $\lambda_1 \geq -1.5$. The grey shaded area corresponds to the integral in Eq. 11. The parameters are the same as in Fig. 2(c).

properties are fully determined by the modulational instability frequency and the damping rate of the filtering.

As PC spectrum provides an adequate approximation, we use it to further analyze the spectral properties and we define the average distance of the spectrum Eq. (7) to the imaginary axis D, which is illustrated in Fig. 4. It is defined as

$$D = \frac{1}{\lambda_0^- - \lambda_0^+} \int_{\lambda_0^-}^{\lambda_0^+} \lambda_1 \, d\lambda_0, \tag{11}$$

where $\lambda_0^- > 0$ and $\lambda_0^+ > 0$ are the lower and upper bounds of the averaging interval. As shown below, this quantity is a useful measure of trends in the memory capacity of RC systems and contrary to the measures introduced in Ref.[26], D does not require to numerically solve the transcendental characteristic equation Eq. (5), which has an infinite number of solutions.

Figure 5 shows the measure D computed in the (η, P) plane for the three values of τ_L (1, 7.5, and 10). The dashed region corresponds to where the equilibrium loses its asymptotic stability. We observe that the upper cut-off frequency significantly affects both the contour of the stability region and the measure D. The smallest values of D are obtained for τ_L=7.5, and consistently to what we had observed in Ref. 11, close to the stability boundary.

In the next part we calculate the memory capacity of the system, and find that the measure D enables one to trace the effect of the eigenvalue spectral shape on the memory capacity. We propose that for the estimation of memory capacity trends, the measure D can be an effective addition to the measure proposed in[26] which is based on the the average distance reduction during the input symbol time.

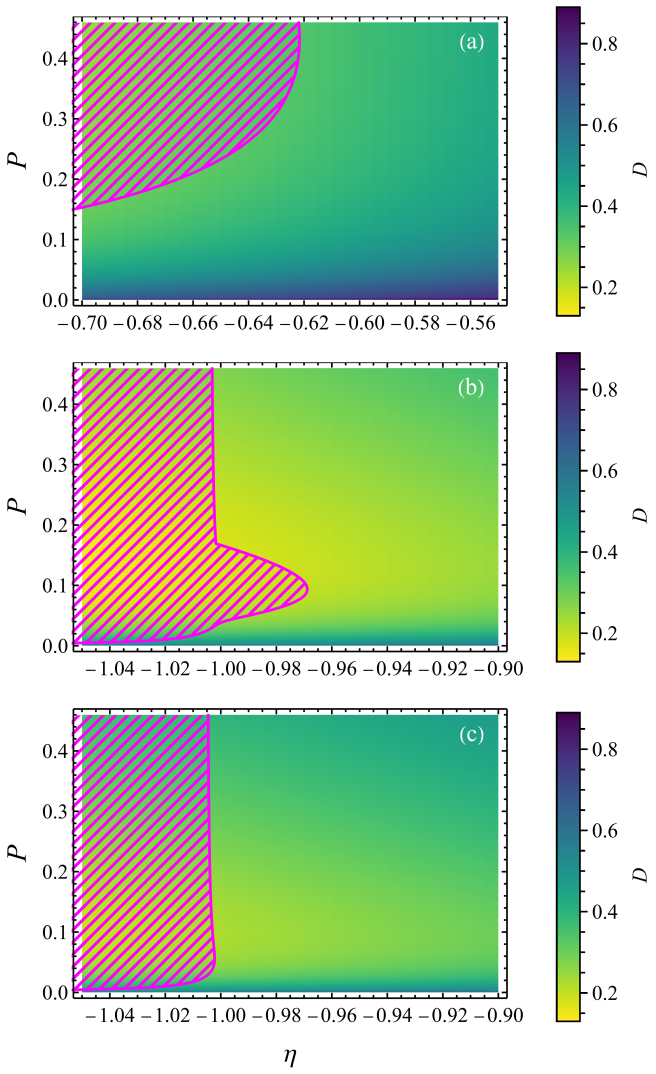

FIG. 5. 2D maps of the average distance from the pseudo-continuous spectrum to the imaginary axis (measure D defined by Eq. (11)), from top row to bottom: (a) $\tau_L = 1$; (b) $\tau_L = 7.5$; (c) $\tau_L = 10$. The dashed region corresponds to the asymptotically unstable spectrum where $\lambda_1 > 0$, and the magenta line is the border of this region. The interval $[\lambda_0^-, \lambda_0^+]$ is defined as in Fig. 4. The other parameters are given in the text.

IV. MEMORY CAPACITY

Memory capacity (MC) measures the ability of the RC system to reproduce the input at previous delay times, and as such is a measure of the performance of the RC. The reservoir's MC is calculated as[28]

$$MC = \sum_{m=1}^{\infty} mc_m = \sum_{m=1}^{\infty} \frac{cov^2(O_i, S_{i-m})}{\sigma^2(S_i)\sigma^2(O_i)}, \qquad (12)$$

where mc_m is the memory function, σ^2 is the variance, cov is the covariance, O_i is the output data value at i-th time-step, S_{i-m} is the input data value delayed by m time-steps.

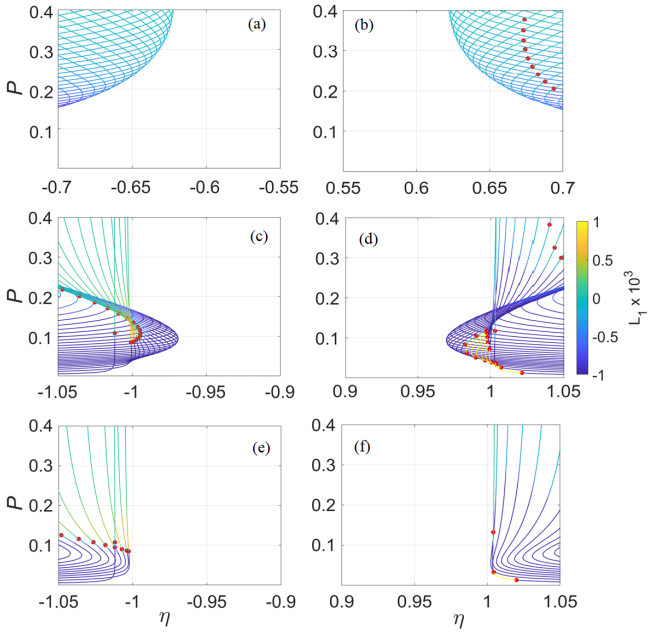

FIG. 6. Hopf bifurcation boundaries, from top row to bottom: (a,b) τ_L = 1; (c,d) τ_L = 7.5; (e,f) τ_L = 10. Color bar is for the Lyapunov coefficients L_1. Red circles indicate $L_1 = 0$. The other parameters are given in the text.

It is known that optimal performance of RC are usually expected in the vicinity of instability from an equilibrium point, typically a Hopf bifurcation in our laser with OE feedback. As a result, we will analyse the bifurcation structure of our free-running time delay systems to provide a dynamical interpretation of TDRC's memory capacity. We determine the Hopf bifurcation structure by means of the DDE-Biftool[29] software and we analyze the evolution of the structure depending on the choice of the low-pass cut-off time-scale τ_L. The results are shown in Fig. 6. We note that the Hopf bifurcation boundaries changes significantly with the variation of the cut-off frequency. The bifurcation has either supercritical or subcritical character, and the first Lyapunov coefficient may substantially change along the boundaries. The ranges of the feedback strength η and the pump parameter P for the RC system's numerical modelling, and used in Fig. 6, are chosen based on the calculated bifurcation boundary for each low-pass filter cut-off time scale τ_L.

Figure 7 shows the 2D maps of the system's MC in terms of the pump parameter P and the feedback strength η, close to the bifurcation borders, for the different values of τ_L along with the Hopf bifurcation borders.

A decrease of the cut-off frequency of the low-pass filter in the feedback loop leads to an increase in MC. The maximum values are observed in the vicinity of the Hopf bifurcation border and for the intermediate value $\tau_L = 7.5$. However, we did not find any pronounced dependency of MC on the Hopf bifurcation character (super- or sub-critical). While the filter bandwidth may significantly affect MC, the variation of the pump current P and the feedback strength η demonstrate a much less significant impact. A similar behavior has been

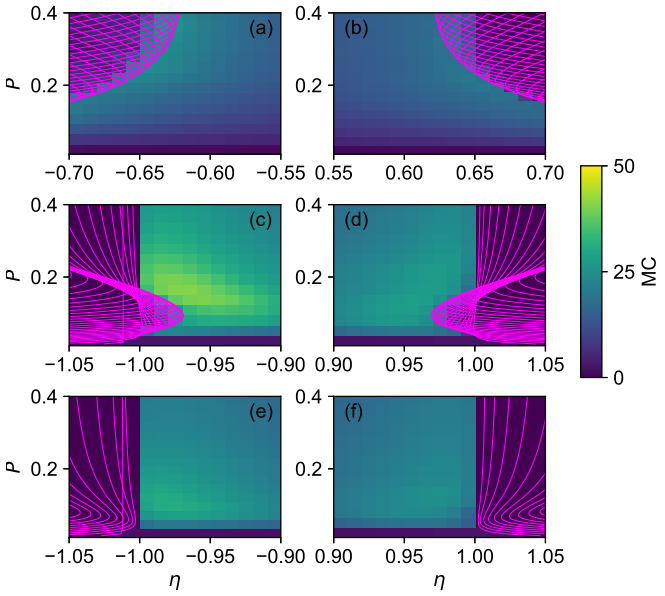

FIG. 7. 2D maps of the system's memory capacity, from top row to bottom: (a,b) $\tau_L = 1$; (c,d) $\tau_L = 7.5$; (e,f) $\tau_L = 10$. The magenta lines are the Hopf bifurcation borders. The other parameters are given in the text.

observed in a RC based on a semiconductor laser and a short external cavity, where *MC* either remains almost constant or slightly increases with the feedback strength increase[30]. A comparison between Figs. 5 and 7 shows that the area with the largest values of *MC* for each τ_L corresponds to the area with the smallest values of measure *D*, further confirming its usefulness as a predictor of the performance of the RC in terms of *MC*. Consistent with observations from Ref. 26, *MC* is maximized when many of the system's eigenvalues have real parts close to zero. Of note, the eigenvalue spectra represented in Fig. 2 correspond to the values of η and *P* that maximize *MC*, and thus minimize *D*, for each value of τ_L. The asymmetry with respect to the feedback sign is observed in our 2D maps of *MC*, and the maximum value of *MC* is obtained for the negative value of feedback strength η for each τ_L (as in Ref. 11).

At the bifurcation border, *MC* for the negative feedback is on the average 1.3 times lager than for the positive one and the strongest asymmetry is observed for $\tau_L = 7.5$.

Finally, we compute the Pearson correlation coefficient $r(MC, D)$ between the average distance *D* and *MC* values obtained from simulation, per the formula

$$r(X,Y) = \frac{cov(X,Y)}{\sigma(X)\sigma(Y)}. \tag{13}$$

Figure 8 shows the correlation scatter plots *MC* vs. *D* for the asymptotically stable parameter ranges, and values of *D* were computed at grid points where *MC* was calculated. As the PC spectrum does not depend on the sign of η, we compare two feedback signs separately. The correlation coefficient varies from -0.93 to -0.97 confirming the possibility to infer *MC* properties from the measure *D*.

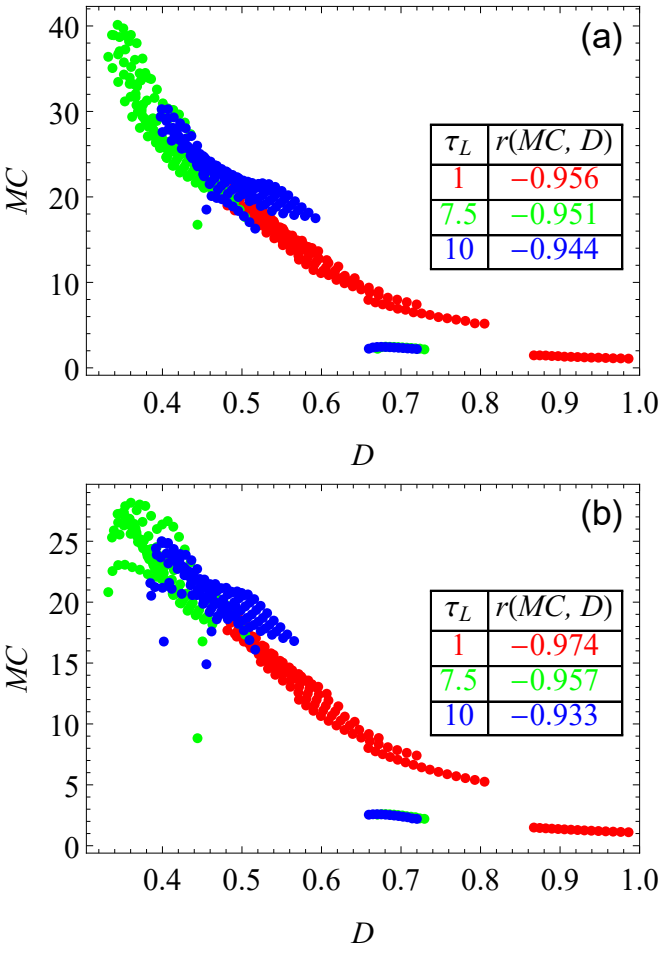

FIG. 8. The correlation scatter plots *MC* vs. *D* for negative (a) and positive (b) feedback signs. The color corresponds to a value of the low-pass filtering parameter: $\tau_L = 1$ (red); $\tau_L = 7.5$ (green); $\tau_L = 10$ (blue). The Pearson correlation coefficient values *r* are given in the insets.

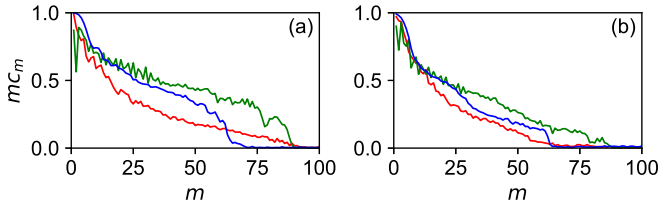

FIG. 9. The memory curve for negative (a) and positive (b) feedback: *m* is the number of delayed input steps for $\tau_L = 1$ (red); $\tau_L = 7.5$ (green); $\tau_L = 10$ (blue). The other parameters are the same as in Fig.2.

We examine in Fig. 9 the memory curves, which are the memory functions mc_m vs the delayed input steps *m*. We conclude that the maximal *MC* results from the flattening of mc_m. The memory depth, which is the delayed input step for which mc_m drops to a value close to zero, is also slightly larger for the optimal value of the low-pass cut-off frequency, and, therefore, partly contributes to the maximal *MC* for $\tau_L = 7.5$.

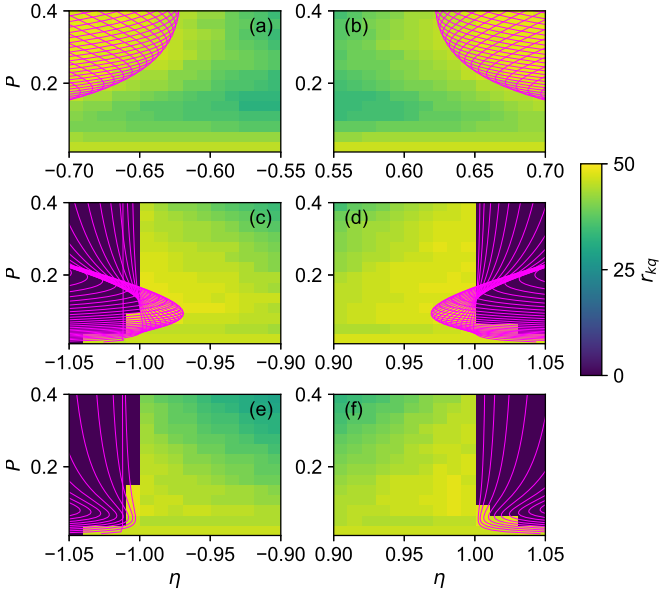

FIG. 10. 2D maps of the system's kernel rank, from top row to bottom: (a,b) $\tau_L = 1$; (c,d) $\tau_L = 7.5$; (e,f) $\tau_L = 10$. The other parameters are given in the text.

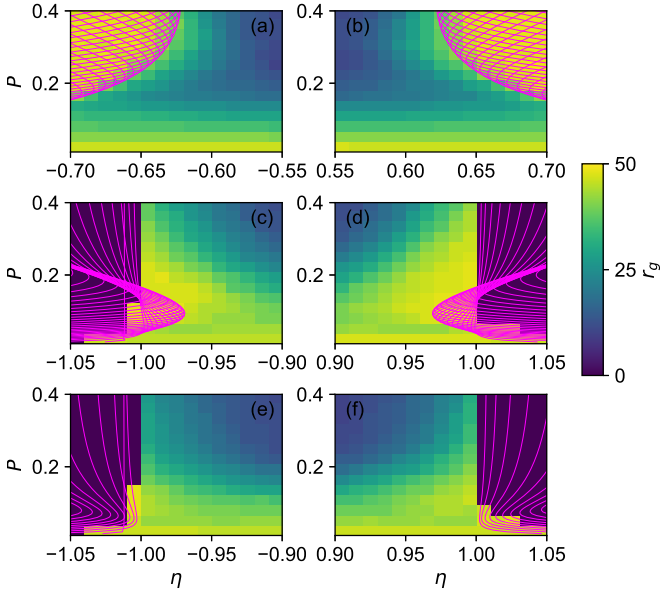

FIG. 11. 2D maps of the system's generalization rank, from top row to bottom: (a,b) $\tau_L = 1$; (c,d) $\tau_L = 7.5$; (e,f) $\tau_L = 10$. The other parameters are given in the text.

V. COMPUTATIONAL ABILITY

Computational ability (*CA*) accounts for both the ability to separate and sufficiently generalize the input data[28]. We calculated it as a difference between the kernel quality rank r_{kq} and a generalization rank r_g, and normalized this value by the number of nodes N

$$CA = \frac{r_{kq} - r_g}{N}, \tag{14}$$

where r_{kq} is the kernel quality rank, r_g is the generalization rank. The kernel rank r_{kq} demonstrates how linearly independent the reservoir is, *i.e.*, how well the RC can discern various input values. A larger value of r_{kq} means an RC would possess more degrees of freedom available for the linear readouts.

The generalization rank r_g quantifies the reservoir's ability to map nonlinearly and consistently distinct inputs to distinct reservoir's states. For the details on how to evaluate these ranks see Ref. 28. The 2D maps of the kernel rank and the generalization rank are given in Figs. 10 and 11 respectively. Both ranks are maximized near the Hopf bifurcation border and decrease away from it. Overall, kernel rank demonstrates smoother profile and low variability across the parameter plane while the generalization rank shows a sharp decline away from the bifurcation border. This decline results in the increase of *CA*.

The 2D maps of systems's *CA* in Fig. 12 demonstrate that the change of cut-off frequency of the low-pass filter leads to a small enhancement of *CA*, with maximal values obtained once again for the intermediate value τ_L. However, contrary to what happens for *MC*, *CA* decreases in the immediate vicinity of the Hopf bifurcation borders, as the maximum is obtained at a relatively small, finite, distance from the borders. In addition, the maximal *CA* value is reached for positive feedback,

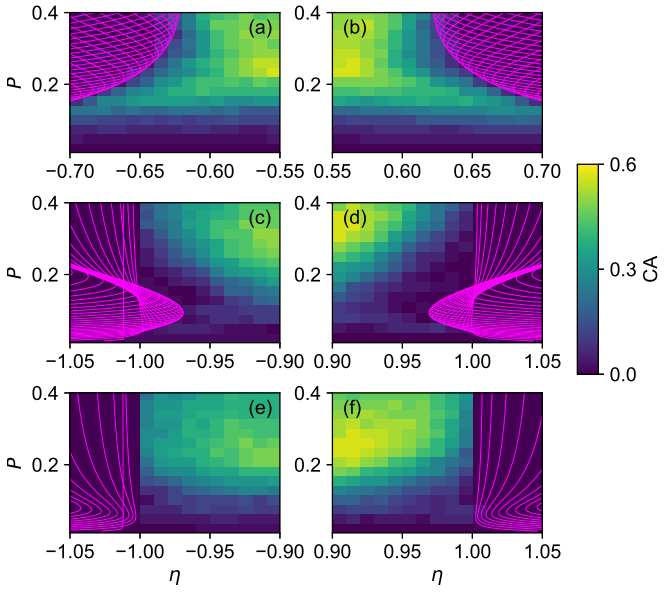

FIG. 12. 2D maps of the system's computational ability, from top row to bottom: (a,b) $\tau_L = 1$; (c,d) $\tau_L = 7.5$; (e,f) $\tau_L = 10$. The other parameters are given in the text.

contrary to the case of *MC*. Overall, we observe a limited impact of feedback filtering on *CA* when compared to its effect on *MC*.

The correlation scatter plots in Fig. 8 confirm a strong linear relationship between *MC* and *D* for all the values of τ_L and both feedback signs. Similar plots for *CA* in Fig. 13 are significantly different: they do not indicate a general trend for correlation and do not provide any evidence of a sustained linear relationship between *CA* and *D*.

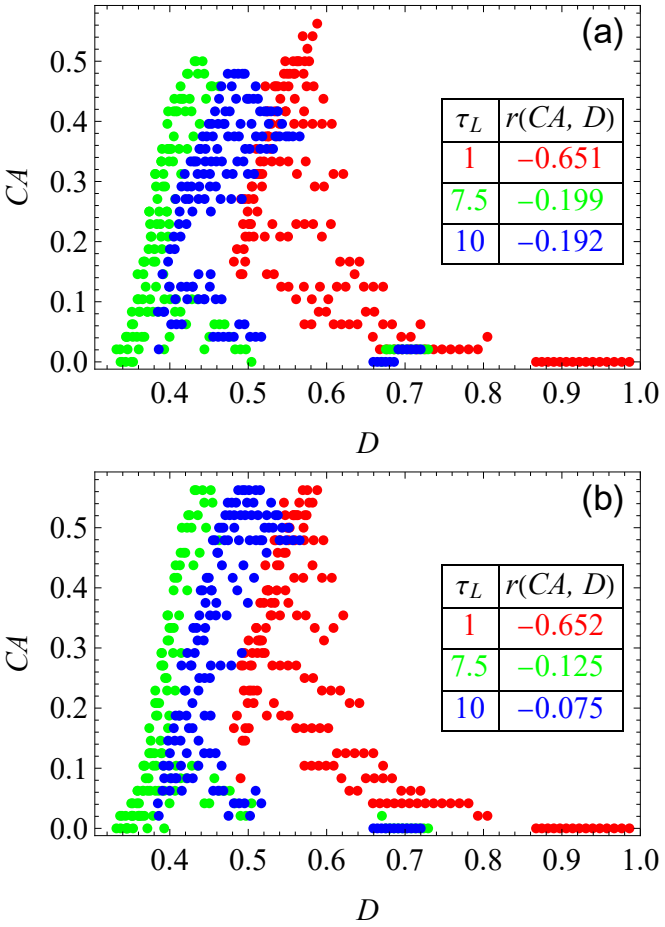

FIG. 13. The correlation scatter plots CA vs. D for negative (a) and positive (b) feedbacks. The color corresponds to a value of the low-pass filtering parameter: $\tau_L = 1$ (red); $\tau_L = 7.5$ (green); $\tau_L = 10$ (blue). The Pearson correlation coefficient values r are given in the insets.

VI. CONCLUSION

In this study, we have shown that altering the low-pass filter cut-off frequency profoundly changes the bifurcation structure and the eigenvalue spectrum of a reservoir computing system based on a laser with optoelectronic feedback. As this frequency is decreased well below the relaxation oscillations frequency, the memory capacity and computational ability tend to increase before decreasing again. Optimum performance is observed for an intermediate value of the cut-off frequency, where a compensation between modulational instability and filtering effects occurs. In this case, the filter leads to significant modification of the damping timescales and therefore of the small signal response of the system manifested by the appearance of a large number of eigenvalues having having nearly equal real parts. Interplay between modulational instability and filtering can thus make numerous eigenvalues, well beyond those involved in modulational instability, be just below the imaginary axis and contribute to the memory of the system for different timescales. We find indeed that the reduction of the distance between the pseudo-continuous spectrum and the imaginary axis correlates well with an increase in memory capacity of a time-delay OE feedback reservoir computer. Computational ability can also be tuned with filtering, but the effect is limited. In conclusion, careful design of filtering properties can thus lead to significant improvement in the memory of a reservoir computer and we expect related improvement in memory-intensive tasks.

ACKNOWLEDGMENTS

The work of A. V. Kovalev and G. O. Danilenko was supported by the Ministry of Science and Higher Education of the Russian Federation under Grant MK-1788.2022.1.2. The work of E. A. Viktorov was supported by the Ministry of Science and Higher Education of the Russian Federation under Grant 2019-1442. D. Rontani gratefully acknowledges the support of the Chair in Photonics. E. A. Viktorov and G. O. Danilenko thank the Professor@Lorraine and Master@Lorraine programs of LUE. A. Locquet and D. S. Citrin acknowledge the support of Conseil Régional Grand Est.

[1] H. Jaeger and H. Haas, "Harnessing Nonlinearity: Predicting Chaotic Systems and Saving Energy in Wireless Communication," Science **304**, 78–80 (2004).
[2] M. Lukoševičius and H. Jaeger, "Reservoir computing approaches to recurrent neural network training," Computer Science Review **3**, 127–149 (2009).
[3] G. Tanaka, T. Yamane, J. B. Héroux, R. Nakane, N. Kanazawa, S. Takeda, H. Numata, D. Nakano, and A. Hirose, "Recent advances in physical reservoir computing: A review," Neural Networks **115**, 100–123 (2019).
[4] G. Van Der Sande, D. Brunner, and M. C. Soriano, "Advances in photonic reservoir computing," Nanophotonics **6**, 561–576 (2017).
[5] A. Lugnan, A. Katumba, F. Laporte, M. Freiberger, S. Sackesyn, C. Ma, E. Gooskens, J. Dambre, and P. Bienstman, "Photonic neuromorphic information processing and reservoir computing," APL Photonics **5**, 020901 (2020).
[6] B. Schrauwen, M. D'Haene, D. Verstraeten, and J. V. Campenhout, "Compact hardware liquid state machines on FPGA for real-time speech recognition," Neural Networks **21**, 511–523 (2008).
[7] J. Torrejon, M. Riou, F. A. Araujo, S. Tsunegi, G. Khalsa, D. Querlioz, P. Bortolotti, V. Cros, K. Yakushiji, A. Fukushima, H. Kubota, S. Yuasa, M. D. Stiles, and J. Grollier, "Neuromorphic computing with nanoscale spintronic oscillators," Nature **547**, 428–431 (2017).
[8] L. Appeltant, M. C. Soriano, G. Van Der Sande, J. Danckaert, S. Massar, J. Dambre, B. Schrauwen, C. R. Mirasso, and I. Fischer, "Information processing using a single dynamical node as complex system," Nature Communications **2**, 1–6 (2011).
[9] D. Brunner, M. C. Soriano, C. R. Mirasso, and I. Fischer, "Parallel photonic information processing at gigabyte per second data rates using transient states," Nature Communications **4**, 1–7 (2013).
[10] A. Argyris, J. Bueno, and I. Fischer, "Photonic machine learning implementation for signal recovery in optical communications," Scientific Reports **8**, 1–13 (2018).
[11] P. S. Dmitriev, A. V. Kovalev, A. Locquet, D. Rontani, and E. A. Viktorov, "Asymmetrical performance of a laser-based reservoir computer with optoelectronic feedback," Optics Letters **45**, 6150–6153 (2020).
[12] L. Larger, M. C. Soriano, D. Brunner, L. Appeltant, J. M. Gutierrez, L. Pesquera, C. R. Mirasso, and I. Fischer, "Photonic information processing beyond Turing: an optoelectronic implementation of reservoir computing," Optics Express **20**, 3241–3249 (2012).
[13] Y. Paquot, F. Duport, A. Smerieri, J. Dambre, B. Schrauwen, M. Haelterman, and S. Massar, "Optoelectronic Reservoir Computing," Scientific Reports **2**, 287 (2012).
[14] F. Duport, A. Smerieri, A. Akrout, M. Haelterman, and S. Massar, "Fully analogue photonic reservoir computer," Scientific Reports **6**, 1–12 (2016).

[15]K. Harkhoe, G. Verschaffelt, A. Katumba, P. Bienstman, and G. Van der Sande, "Demonstrating delay-based reservoir computing using a compact photonic integrated chip," Optics Express **28**, 3086–3096 (2020).
[16]A. Argyris, J. Bueno, and I. Fischer, "PAM-4 Transmission at 1550 nm Using Photonic Reservoir Computing Post-Processing," IEEE Access **7**, 37017–37025 (2019).
[17]J. Vatin, D. Rontani, and M. Sciamanna, "Experimental realization of dual task processing with a photonic reservoir computer," APL Photonics **5**, 086105 (2020).
[18]D. Brunner, B. Penkovsky, B. A. Marquez, M. Jacquot, I. Fischer, and L. Larger, "Tutorial: Photonic neural networks in delay systems," Journal of Applied Physics **124**, 152004 (2018).
[19]P. Antonik, N. Marsal, D. Brunner, and D. Rontani, "Bayesian Optimisation of Large-scale Photonic Reservoir Computers," Cognitive Computation , 1–9 (2021).
[20]J. Nakayama, K. Kanno, and A. Uchida, "Laser dynamical reservoir computing with consistency: an approach of a chaos mask signal," Optics Express **24**, 8679–8692 (2016).
[21]J. Boedecker, O. Obst, J. T. Lizier, N. M. Mayer, and M. Asada, "Information processing in echo state networks at the edge of chaos," Theory in Biosciences **131**, 205–213 (2012).
[22]J. Bueno, D. Brunner, M. C. Soriano, and I. Fischer, "Conditions for reservoir computing performance using semiconductor lasers with delayed optical feedback," Optics Express **25**, 2401–2412 (2017).
[23]Y. Kuriki, J. Nakayama, K. Takano, and A. Uchida, "Impact of input mask signals on delay-based photonic reservoir computing with semiconductor lasers," Optics Express **26**, 5777–5788 (2018).
[24]M. S. Islam, M. S. Islam, A. V. Kovalev, G. Coget, E. A. Viktorov, D. S. Citrin, D. S. Citrin, A. Locquet, and A. Locquet, "Staircase dynamics of a photonic microwave oscillator based on a laser diode with delayed optoelectronic feedback," Physical Review Applied **13**, 064038 (2020).
[25]T. Erneux and P. Glorieux, Laser Dynamics, Vol. 9780521830 (Cambridge University Press, 2010).
[26]F. Köster, S. Yanchuk, and K. Lüdge, "Insight into delay based reservoir computing via eigenvalue analysis," Journal of Physics: Photonics **3**, 024011 (2021).
[27]S. Yanchuk and M. Wolfrum, "A multiple time scale approach to the stability of external cavity modes in the Lang-Kobayashi system using the limit of large delay," SIAM Journal on Applied Dynamical Systems **9**, 519–535 (2010).
[28]L. Appeltant, J. Danckaert, I. Fischer, and G. V. D. Sande, "Reservoir computing based on delay-dynamical systems," These de Doctorat, Vrije Universiteit Brussel/Universitat de les Illes Balears (2012).
[29]K. Engelborghs, T. Luzyanina, and D. Roose, "Numerical bifurcation analysis of delay differential equations using DDE-BIFTOOL," ACM Transactions on Mathematical Software **28**, 1–21 (2002).
[30]K. Takano, C. Sugano, M. Inubushi, K. Yoshimura, S. Sunada, K. Kanno, and A. Uchida, "Compact reservoir computing with a photonic integrated circuit," Optics Express **26**, 29424–29439 (2018).